The Significance of Crystallographic Texture in Dry Etching of Titanium to Engineer Bioinspired Nanostructured Bactericidal Surfaces

ANINDO ROY,[1] SAURABH KUMAR GUPTA,[1] SATYAM SUWAS,[1] and KAUSHIK CHATTERJEE [1,2]

1.—Department of Materials Engineering, Indian Institute of Science, CV Raman Road, Bengaluru 560012, India. 2.—e-mail: kcahatterjee@iisc.ac.in

Titanium is the prevalent material of choice for metallic implantable devices. However, post-operative bacterial infections remain a major cause of implant failure. Mechanobactericidal surfaces have garnered much attention due to their ability to neutralize bacteria, via physical forces and interactions instead of traditional chemical routes. In this work, the texture of titanium substrates was modified via cold rolling, hot rolling, and annealing treatments, and the resultant crystallographic textures were characterized. Subsequently, nanoscale topographies were generated on the substrates via maskless plasma etching. The results indicated the subtle differences in the topographies of substrates with different textures being critical factors affecting the etching process. All the substrates were then assessed for bactericidal activity against *P. aeruginosa* and *S. aureus* bacteria, with killing efficiencies reaching up to 50% for *P. aeruginosa*. The nanostructures were ineffective against *S. aureus* due to the presence of a thick peptidoglycan layer in their cell walls. Detailed statistical analysis showed that, in the case of *P. aeruginosa*, texture plays a significant role in determining the killing efficiency, due to its subtle effects on the etching process and consequently nanostructure dimensions. The results of this study emphasize the importance of material processing in the engineering and development of the next generation of mechanobactericidal surfaces.

INTRODUCTION

Bacterial proliferation, colonization, and subsequent infection on metallic implant surfaces are one of the leading causes of implant failure, accounting for a significant portion of revision surgeries.[1–3] The conventional approach of administering broad-spectrum antibiotics to tackle this issue is becoming increasingly unpopular due to the rise of antimicrobial resistance (AMR), which has led to the emergence of drug-resistant and multidrug-resistant "superbugs". AMR is projected to be responsible for more than 50 million deaths globally by 2050.[4] In the past decade, high aspect ratio nanostructures such as nanopillars were found to possess bactericidal activity, whereby they penetrate the cell membrane and rupture it, killing the bacteria in the process.[3,5] This finding has ushered in a new age in the field of contact-killing surfaces, which is especially promising because such "mechanobactericidal" surfaces do not depend on chemical routes to kill bacteria, and, hence, are not susceptible to the emergence of resistance. Since their discovery on natural surfaces, such as insect wings and gecko skin, researchers around the globe have successfully emulated similar nanotopographies on a wide range of materials, including metals, polymers, and ceramics.[3,6–8]

The fabrication of such mechanobactericidal topographies on clinically relevant materials such as titanium has recently attracted much interest, requiring the application of appropriate

nanofabrication techniques. Dry etching or etching of material surfaces using high energy plasma, a method prevalent in the semiconductor industry, has been demonstrated to be capable of generating such mechanobactericidal topographies on titanium.[9–11] However, the role that the crystallographic texture might play in such processes has not been investigated. Crystallographic texture in a polycrystal has significant effects on its properties, some of which, such as substrate stiffness and wettability, are known to affect cell behavior and cell fate on the substrate, although their effect on bacterial attachment has not been investigated.[12–14] Texture can be used to tune the surface energy of bulk material, as it can help orient low or high surface energy planes with respect to the material surface.[15] Strong texture can also render material properties anisotropic. This can affect etching characteristics during dry etching processes, as the evolution of nanopillars can differ on the different planes of a crystal, owing to their differences in chemical potential or reactivity. More importantly, texture has been reported to play an important role in determining the etch rates and orientations in several materials, such as TiN and diamond, but its role in reactive ion etching (RIE) of titanium has not been reported.[16,17]

In this study, we aimed to investigate the role that crystallographic texture might play on maskless dry etching of titanium and, subsequently, on its bactericidal activity. We subjected titanium to three different processing routes to yield different crystallographic textures, and then generated nanoscale topographies on them via a maskless dry-etching process. Finally, we investigated the bactericidal efficiency (BE) of these surfaces by evaluating the damage caused to the bacterial cell membrane, probed the interactions occurring at the interface between bacteria and nanostructures, and analyzed differences to quantify the roles of texture on the mechanobactericidal activity of nanostructured titanium.

MATERIALS AND METHODS
Preparation and Processing of Ti Substrates

Rectangular slabs (30 mm × 10 mm × 2 mm) of commercially pure titanium (cp-Ti, Grade 2) were first homogenized at 1000 °C for 1 h and used for all further processing. The specimens were rolled to a thickness of 0.6 mm through three different routes (Fig. 1a) before being cut into smaller rectangular pieces for further experiments and characterization. Hot rolling (HR) was performed in the α phase at 800 °C $\varepsilon_t = 0.1$ per pass, whereas unidirectional cold rolling (CR) was performed at room temperature (25 °C) with $\varepsilon_t = 0.02$ per pass (60 passes). Finally, the CR samples were annealed (CR + A) after coating with Deltaglaze before placing them in a furnace at 750 °C to prevent the formation of the alpha casing. The coating was removed by pickling

the rolled samples in an acidic solution. Post-rolling, the sample surfaces were polished using emery papers with grit sizes up to 3000, followed by electropolishing (Struers Lectropol-5; Denmark) at 40 V for 20 s in A3 solution to achieve a mirror finish. These samples were used for all further characterization and experiments.

Microstructure and Crystallographic Texture Analysis

The microstructure of all the sample groups was characterized using an optical microscope (Leica systems) on a plane perpendicular to the transverse direction (TD) of the rolled sheet. Post-metallographic preparation, the sample surfaces were etched by immersing them in Kroll's reagent for 20 s, followed by rinsing in copious amounts of fresh water. The samples were then blow-dried using air and imaged.

The bulk texture of the samples was measured by an x-ray texture goniometer (Bruker D8 Discover) in Schulz reflection geometry using Co-Kα radiations. Six incomplete pole figures, 10.0, 00.2, 10.1, 10.2, 11.0, and 10.3, were measured using a 2.5° × 2.5° grid size and 3 s per step. The samples were oscillated in the x and y directions with 1 mm amplitude and 1 mm s^{-1} speed. Data from these measurements were used to calculate the orientation distribution function (ODF) using the commercially available LaboTex software (LaboSoft, Krakow, Poland), and, subsequently, the ODFs were used to generate a complete (0002) pole figure for textural analysis.

Reactive Ion Etching

The polished titanium samples were sonicated in ethanol, acetone, and deionized water for 5 min each to remove contaminants from the surface, and then dried in air. Next, the samples were placed on a SiO$_2$ wafer and fixed using thermal grease (aluminum nitride) to prevent sample movement during handling, and to facilitate heat transfer and cooling during the etching process. The samples were etched using maskless chlorine-based recipes in an inductively coupled plasma reactive ion etching (ICP-RIE) system (Plasmalab System 100; Oxford Instruments, UK).[11] The system uses an ICP coil to dissociate gas molecules and generate ions, which are then accelerated towards the substrate placed on the lower electrode by applying a DC bias to the latter. Both the ICP coil and the lower electrode are powered using radio frequency (RF) generators. In this study, the ICP and RF powers were set at 1000 W and 50 W, respectively. The feed gas composition was maintained at 100% Cl$_2$ introduced at a flow rate of 30 sccm into the reaction chamber, while the chamber pressure was maintained at 3 mTorr for all runs. The samples were etched for 5 min, 10 min, and 15 min to generate nanopillars on the sample surfaces. All

The Significance of Crystallographic Texture in Dry Etching of Titanium to Engineer
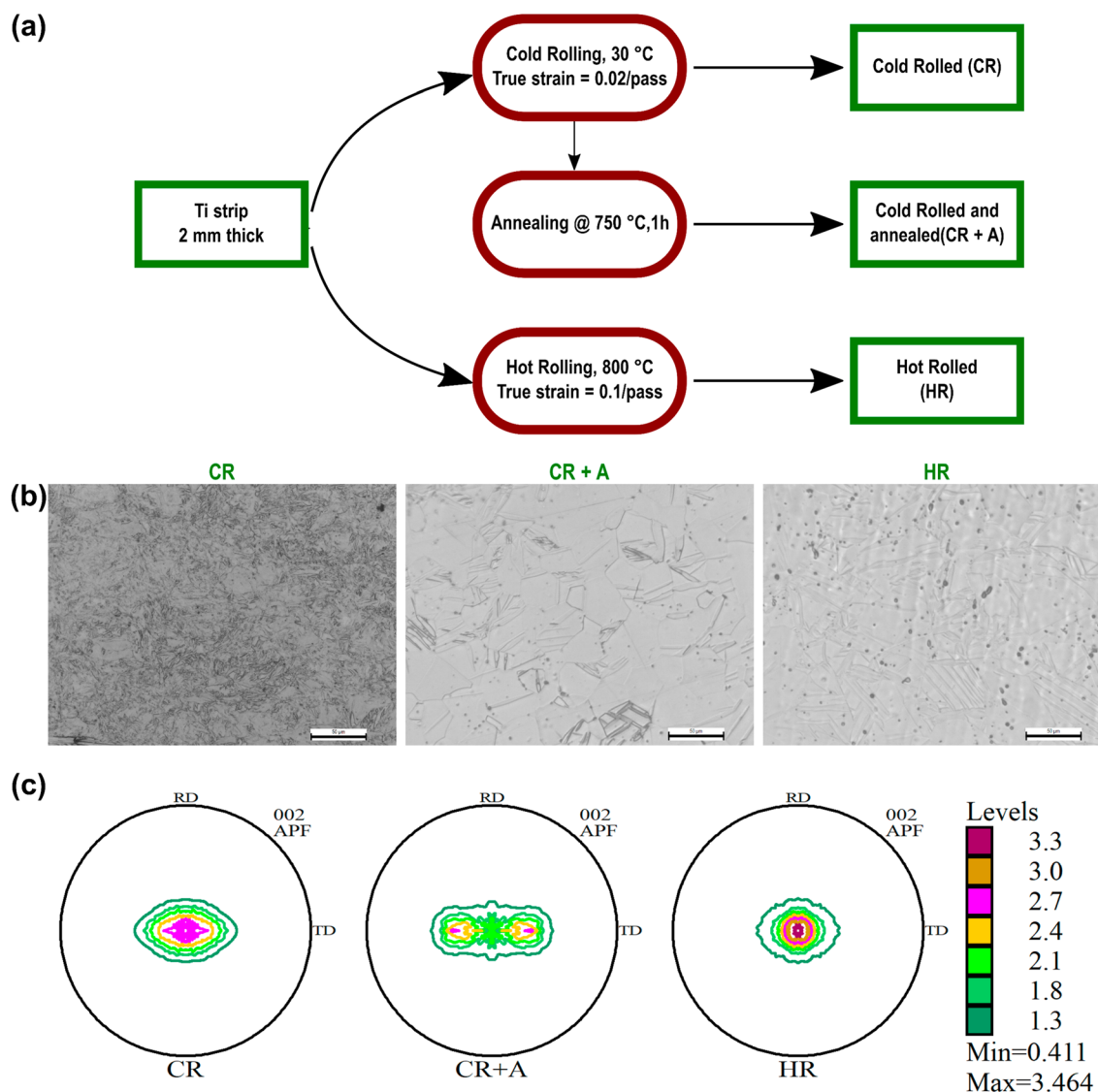Bioinspired Nanostructured Bactericidal Surfaces

3369

Fig. 1. (a) The different processing routes the titanium was subjected to in this study, (b) optical micrographs of the titanium samples post-processing, and (c) (0002) pole Figs of titanium samples generated from x-ray texture measurement data.

unetched control and black titanium surfaces were cleaned in isopropyl alcohol, acetone, and ethanol prior to characterization and biological study.

Characterization of Nanostructured Surfaces

Scanning Electron Microscopy

The micro-/nano-topography on the titanium surfaces was characterized using a FESEM (Ultra 55 FESEM; Carl Zeiss, Germany) operated at 5 kV, and micrographs were captured using an in-lens detector at magnifications ranging from $\times 5000$ to $\times 80,000$. At least three different regions of each sample were imaged to ensure the uniformity of features throughout the sample.

Atomic Force Microscopy

The surface topography of the control and CR + A samples was evaluated in air using an atomic force microscope (Dimension Icon, ScanAsyst; Bruker, Germany) operated in non-contact mode at room temperature. A silicon micro-cantilever (ACTA; AppNano, USA), with a nominal spring constant of 37 N/m and a resonance frequency of 300 kHz, was used to scan at least two 5×5 μm^2 areas for each sample. The open-source software Gwyddion (v.2.46) was used to analyze and plot the data.

X-ray Diffraction

X-ray diffraction (XRD) profiles were measured using an x-ray diffractometer (Rigaku Smart Labs) with Cu-Kα radiation ($\lambda = 0.15406$ nm). Measurements were conducted over an angular range of 30–80°, with a step size of 0.016° per s under ambient conditions. The data were plotted and analyzed using X'pert Highscore software.

Bacterial Culture

Stock solutions of the Gram-negative *Pseudomonas aeruginosa* (ATCC 27853) and Gram-positive *Staphylococcus aureus* (ATCC 25923) bacterial strains were prepared in nutrient broth (Oxoid; Thermo Fisher Scientific, Australia) and stored at $-20\,°C$ until use. Prior to the experiments, stock suspensions were refreshed on nutrient agar (Oxoid; Thermo Fisher Scientific) at $37\,°C$ for 24 h. Fresh bacterial cultures were prepared by inoculating a single colony from plate culture in 10 ml of nutrient broth and incubating overnight at $37\,°C$. Cells were then collected at the logarithmic stage of growth, and suspensions with an optical density of 0.1 ($OD_{600} = 0.1$) were prepared prior to the experiment by diluting the culture with fresh media. Then, 300 μL aliquot of the bacterial suspension was used to fully submerge each substratum in a sterile 48-well culture plate, which was incubated for 4 h at $37\,°C$ under dark and static conditions. The viability of the adhered bacterial cells was determined by staining the cells with the L7012 LIVE/DEAD BacLight Bacterial Viability kit (Molecular Probes, Invitrogen, USA) following the manufacturer's protocol. Briefly, post-incubation, non-adherent bacteria were removed by removing the bacterial suspension from the wells and washing the samples thrice using phosphate,-buffered saline (PBS). Cells adhered to the substrate were then stained using a 1:1 mixture of 3.3 mM SYTO 9 and 20 mM propidium iodide for 15 min at room temperature. Post-staining samples were gently washed once again using PBS solution to remove excess dye solution and then imaged with a fluorescence microscope (IX-53 microscope, Olympus, Japan) at $20 \times$ magnification in the green and red channels for the live and dead cells, respectively. Cell viability was determined by counting the cells stained both green and red from three images of at least three independent replicates.

The metabolic activity of the cells on the flat and the nanostructured surfaces (NSSs) was evaluated using the Alamar Blue assay (Thermo Scientific). After 4 h of incubation, the samples were washed thrice with PBS as described above and then incubated in a solution containing 0.015 mg/ml dye for 4 h at $37\,°C$. Then, the dye solution was collected, and the fluorescence intensity was recorded with a spectrophotometer (Biotek) at absorption and emission wavelengths of 530 and 590 nm, respectively. All measurements were carried out in triplicate.

Bacterial Cell Morphology and Attachment Patterns

To assess the morphology of the bacterial cells, the samples with adhered cells were observed by FESEM using an SE2 detector. Prior to imaging, the cells were affixed using 2.5% glutaraldehyde solution for 1 h at room temperature. Then, the cells

were dehydrated via immersion in 30, 50, 70, 90, and 100% ethanol solution for 10 min each. The samples were finally air-dried and subsequently coated with gold using a gold coater (Quorum 150R; Quorum Technologies, UK) for 120 s to avoid charging of the samples during imaging.

Statistical Analysis

The statistical significance of the two independent variables, namely the crystallographic texture of the sample and differences in nanopillar dimensions due to different etching times, were evaluated using the two-way ANOVA test in Prism software (v.8.4.0; GraphPad, USA). Subsequently, Tukey's multiple comparisons test was performed to compare differences between the means of the different experimental groups, and p values < 0.05 were considered statistically significant.

RESULTS AND DISCUSSION

The titanium samples displayed three distinctly different microstructures post-processing, depending on the processing route (Fig. 1a, b). The microstructure of the CR sample showed severely deformed grains with high aspect ratios characteristic of cold-rolled samples. In contrast, the annealed counterpart (CR + A) sample exhibited a completely recrystallized microstructure, with large equiaxed grains. This occurs due to prolonged holding of the sample at high temperatures, in the grain-growth regime, during the annealing process. The HR sample exhibited a partially recrystallized microstructure, with a mixture of relatively large equiaxed and elongated smaller grains. This is likely produced by dynamic recrystallization during hot rolling in the α-phase. Both the HR and CR + A samples show the presence of deformation twins.

During plastic deformation in a polycrystalline material, grains that are oriented randomly, to begin with, undergo slip and rotation in a complex fashion to arrive at another orientation. The new orientations are determined by the deformation conditions. This leads to the formation of a crystallographic texture in polycrystalline materials, which is measured by pole figures. The (0002) pole figures of all the samples were measured to characterize the crystallographic texture evolved as a result of the processing routes chosen for this study. ODFs were generated from the six measured incomplete pole figures. Furthermore, the complete pole figures were calculated from the ODFs (Fig. 1-c). The volume fractions of the basal fibers for respective samples, as calculated from the ODFs with an orientation spread of 15° in three Euler's angles, $\varphi1$, φ, and $\varphi2$, are presented in Table I. In the case of HR, the volume fraction of basal fiber is 8.4%, which was the highest among all the processing routes. For CR and CR + A, this value was calculated to be 7.7% and 5.5%, respectively. A split of basal poles toward the TD was 11° and 35° away

Table I. Volume fraction of basal fiber $(0002)[uvtw]$ for different sample conditions

Sample	CR	CR + A	HR
Volume fraction of basal fiber	7.7%	5.5%	8.4%

from the normal direction (ND) is seen in the case of CR and CR + A samples, respectively, which is typical of HCP metals with a c/a ratio <1.633.[12] The split was more pronounced in CR + A samples due to annealing, which caused the basal poles to shift farther apart from the ND towards the TD. In the grain-growth regime, the annealing texture of Ti is reported to be rotated by $\sim 30°$ around the c-axis, and is similar to that of the cold-rolled texture.[18]

Next, nanoscale topographies were successfully generated on Ti substrates with all three different crystallographic textures, via maskless RIE using chlorine plasma. Previously, we have reported that nanopillars during maskless etching of titanium form because of micro-masking of the substrate surface by SiOCl species inside the chamber.[11] The etching process itself is a result of both physical bombardment by chlorine ions and chemical reactions between chlorine and titanium atoms exposed on the substrate surface. The chemical component of the etching process is the more dominant of the two, and the reaction leads to the formation of a volatile etch product, namely $TiCl_4$, which is then desorbed from the surface and pumped out (see Fig. 2a).[11] Post etching, all the surfaces were found to be covered with erect arrays of vertically aligned nanopillars throughout the entire sample (Fig. 2b–d). XRD measurements revealed that no additional phases were formed during the etching process, and that the major constituent phase in both the unetched and nanostructured samples was the α phase of Ti (refer to online supplementary material, Fig. S1). AFM scans of CR + A sample confirmed that an increase in etch duration from 5 to 10 and 15 min resulted in a concomitant linear increase in pillar height, with pillar heights reaching the micron scale after 15 min of etching (Fig. 3b). Tip cluster formation due to collapsing of the pillar tips was noticed in the CR and HR samples etched for 15 min. This occurs due to the high aspect ratios of the nanostructures whereby, due to an increase in pillar height, the pillar structure is no longer capable of maintaining its erect distinct morphology, and the pillars collapse due to gravitational, electrostatic, and other interactions between themselves.[19,20]

Measurements of pillar diameters from the SEM micrographs revealed that all the samples show a bimodal distribution of pillar diameters. In the case of the CR sample, the 5 min and 10 min samples have comparable diameters, with mean diameters of

43 $\pm$ 7 nm and 48 $\pm$ 9 nm, respectively. The sample etched for 15 min exhibited a relatively broader distribution with a mean diameter of 53 nm $\pm$ 10 nm. This is in stark contrast to the HR sample, where, although the 15 min etched sample showed a similarly broad distribution with a mean of 71 nm $\pm$ 9 nm, the 5 min and 10 min etched samples had a narrow, almost unimodal distribution curve with mean diameters of 41 nm $\pm$ 5 nm and 53 nm $\pm$ 6 nm, respectively. The CR + A samples also exhibited a simultaneous increase in pillar diameter, with an increase in etching time with mean diameters of 36 nm $\pm$ 5 nm for the 5 min etch, 52 nm $\pm$ 6 nm for the 10 min etch, and 62 nm $\pm$ 6 nm for the 15 min etch samples. Measurement of pillar interspacing revealed that the HR sample had relatively higher interspacing for both the 5 min (273 nm $\pm$ 32 nm) and 10 min (268 nm $\pm$ 34 nm) etched samples compared to the CR and CR + A samples. However, all the values lie in the range of 150–300 nm, which is comparable to the interpillar spacing in cicada wings. The 15 min etched samples exhibited excessive tip clustering in the case of the CR and HR samples, resulting in an unusually broad distribution and high means. The inter-cluster spacing was 696 nm $\pm$ 158 nm and 779 nm $\pm$ 106 nm for CR and HR, respectively. In contrast, the CR + A sample did not exhibit such excessive tip clustering, and had a mean interspacing of 408 nm $\pm$ 46 nm (Fig. 3b).

This increase in diameter with etch duration occurs because of the interaction of ions with the nanopillars in the latter part of the etch duration. In the beginning, 100% of the incoming ions interact only with the flat sample substrate. As etch duration increases, nanopillars develop, and a significant fraction of the incoming ions start interacting with the pillar tips and etch them in the process. The fraction of ions reaching between the pillars reduces with increasing pillar height due to aspect ratio-dependent etching effects (ARDE). ARDE is a well-known phenomenon whereby the etching rate of structures with higher aspect ratios is lower due to the lower probability of reactive ions reaching the substrate floor.[11] However, in the case of the CR sample, the pillar diameters for all three etching times are comparable, albeit the samples etched for longer durations have higher means and exhibit broader distributions. This may be because of the smaller grain size and high dislocation density in the CR sample, which means the presence of high-energy regions and loosely bound atoms, leading to higher etch rates both in terms of physical sputtering and chemical reactions. Simultaneously, this also means increased etch isotropy compared to the HR or CR + A samples, as sidewall etching or etching of the pillar surfaces will be more dominant in the CR sample. This leads to comparably thinner pillars on the CR 15 min sample than on the other two textured samples.

(a) Chlorine in
Source power
Plasma
Titanium
To pump
Bias power

(b) Top view · 15° inclined view
CR
HR
CR+A

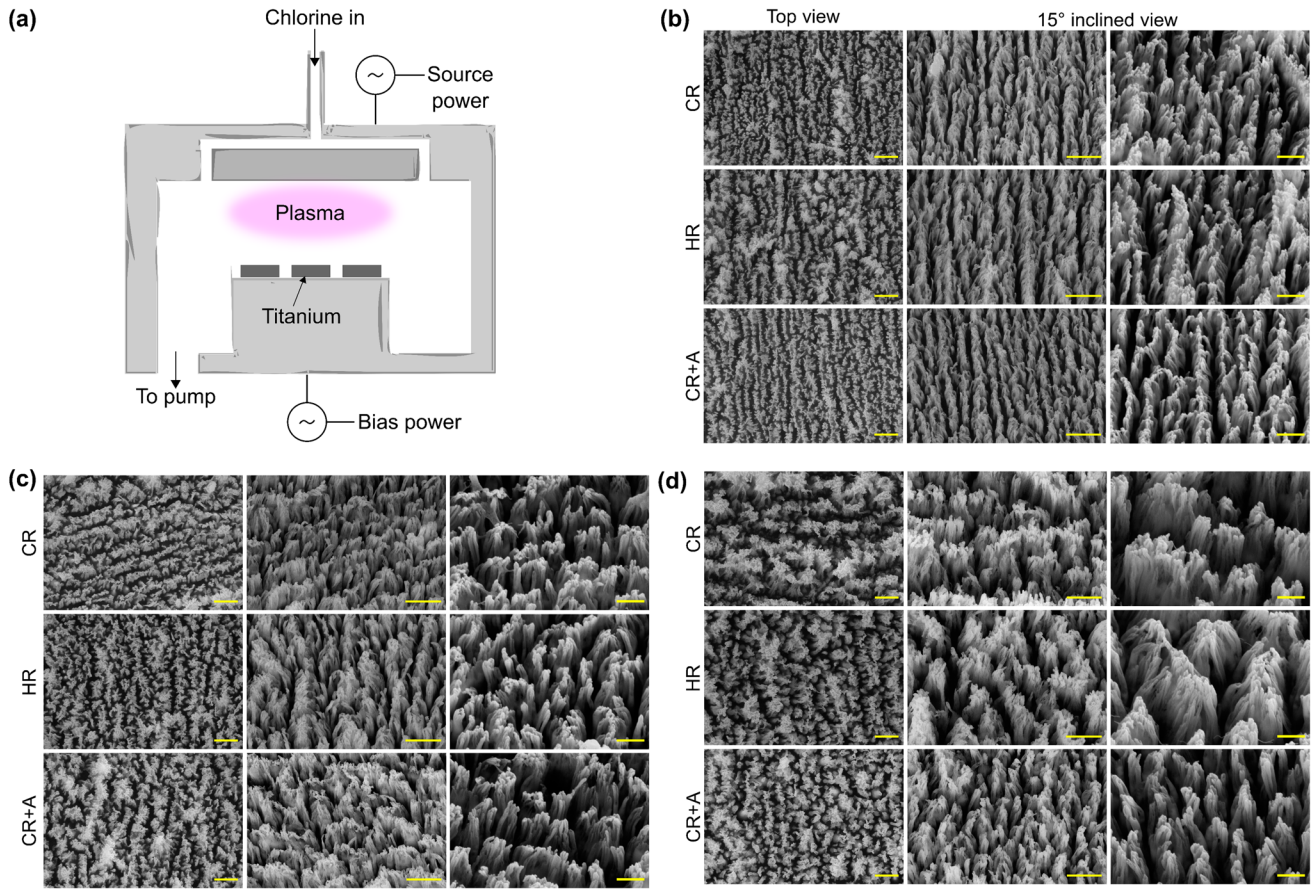**(c)**
CR
HR
CR+A

(d)
CR
HR
CR+A

Fig. 2. (a) Schematic of the ICP-RIE system used for dry etching of titanium substrates; (b–d) topographical characterization of nanostructured Ti surfaces; top-view and 15° inclined view SEM micrographs of the resultant surfaces following (b) 5 min, (c) 10 min, and (d) 15 min of maskless plasma etching; Scale bars 1 μm for the left and middle panels and 500 nm for the right panels.

Post-RIE, the NSSs were exposed to the clinically relevant and well-known pathogens, *P. aeruginosa* and *S. aureus*, for 4 h, to assess their bactericidal activity. *P. aeruginosa* is a Gram-negative opportunistic pathogen with several antibiotic-resistant strains, and is frequently linked to implant-associated bone and joint infections, as well as hospital-related infections worldwide.[21,22] Nanopillars are known to penetrate and rupture the bacterial cell wall, causing the effusion of intracellular fluid and cell death.[3,6,23] Therefore, the viability of the cells was calculated from the analysis of fluorescence micrographs of adhered cells on the flat control and the NSSs (Fig. 4a and b). Analysis and quantification of live and dead cells on these surfaces revealed that the NSSs were successful in killing the bacterial cells. The samples etched for 5 min and 10 min exhibited the highest degree of mechanobactericidal activity for all three texture groups. In the case of the samples etched for 15 min, the killing efficiency was found to be lower. This decrease was more pronounced for the CR and HR samples, which showed more than a twofold drop in the BE. For the CR + A sample, the BE was reduced by more than 10%. The lower BE for the CR and HR 15 min etched samples could be due to the clustering of the

pillar tips. Tip clustering results in fewer attachment points for the bacteria, thereby offering fewer pillars for the interaction with cells and increasing the chances of preferential alignment between tip clusters.[10] Another, and perhaps more important factor, could be that, as the pillar height (and overall aspect ratio) increases with etching time, their tendency to bend or deflect under shear forces applied by the bacteria increases.[24,25] This leads to a reduction in pillar rigidity. Thus, pillars on the 15 min etch samples exerted lower deformation on the cell membrane, as compared to the pillars on samples etched for 5 min and 10 min. This, in turn, led to the greater survivability of the bacteria, which, although not as comfortable as on a flat surface, were able to maintain cell shape integrity. This also explains the reduction of BE for the CR + A 15 min sample. The BE of samples etched for the same duration but belonging to different texture groups was comparable, and differences were within the calculated statistical deviation. It should be mentioned that the differences in BE between different texture groups for the same etch durations were not statistically significant, except in the case of the samples etched for 15 min.

The Significance of Crystallographic Texture in Dry Etching of Titanium to Engineer
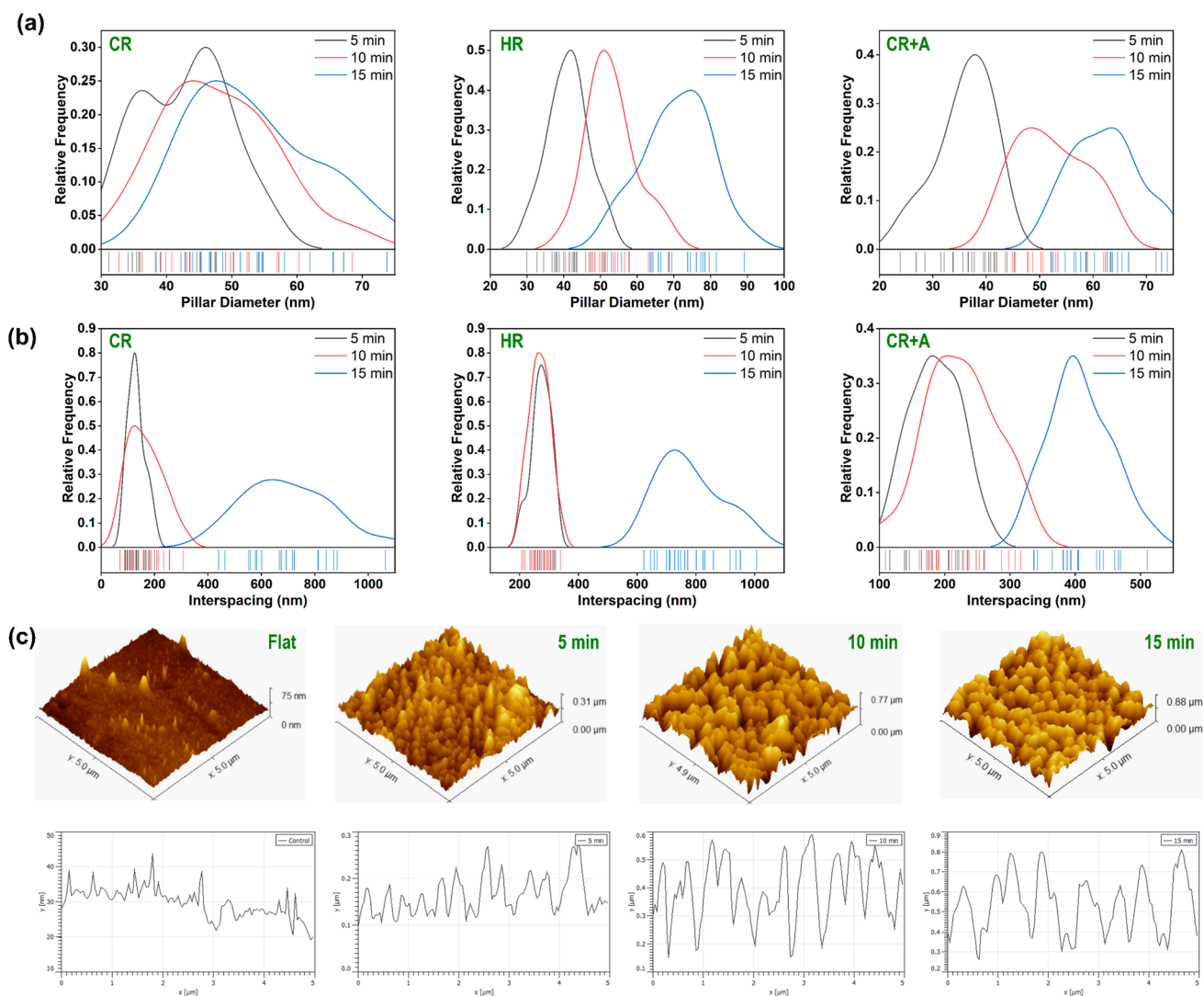Bioinspired Nanostructured Bactericidal Surfaces

3373

Fig. 3. (a) Distribution + rug plots showing pillar diameter distributions for samples etched for different time durations on different textures. (b) Distribution + rug plots showing pillar interspacing for different textures and time durations. For the samples etched for 15 min, interspacing was measured between tip clusters. (c) 3D renditions of AFM scans performed on the annealed flat unetched sample, samples etched for 5 min, 10 min, and 15 min, and their corresponding line plots.

Next, the bacteria–nanostructure interface and the possible interactions between them were probed with the help of SEM. Post-4 h of incubation, cells attached irreversibly on to all the substrates and were found to form microcolonies on the flat unetched surfaces (Fig. 5a). On the NSSs, bacterial cells settled on top of the nanopillars, and interacted with, and adhered to, the pillar tips, as is evident from the deformed morphology of the pillars, as pillars around a bacterial cell were often bent in the direction of the bacteria. Unlike the macroscale world, where inertial forces are largely dominant over viscous forces, bacteria exist in a low Reynolds number universe, where the effects of gravitational forces are insignificant. Thus, the bending of the pillar tips clearly occurs due to shear pull forces exerted by the bacteria in an attempt to attach or move across the NSSs. The exact consequences of these interactions and how this eventually leads to bacterial death is still an active field of research. However, it has been recently demonstrated that elastic strain energy is stored in the nanopillars during the elastic deformation process due to bacterial pull. When this value crosses a certain threshold, the pillar springs back to its original position, stretching and rupturing the cell membrane in the process.[11,25] Indeed, SEM micrographs of several bacterial cells reveal tent-like pinning of the cell membrane (Fig. 5b). This also explains the reduction in BE for the 15 min etched surfaces, since taller pillars are more susceptible to bending compared to their low aspect ratio counterparts.[25] This means that, for a fixed magnitude of tip deflection, the stored elastic energy in a taller pillar is lower in magnitude and thus likely to cause less damage.
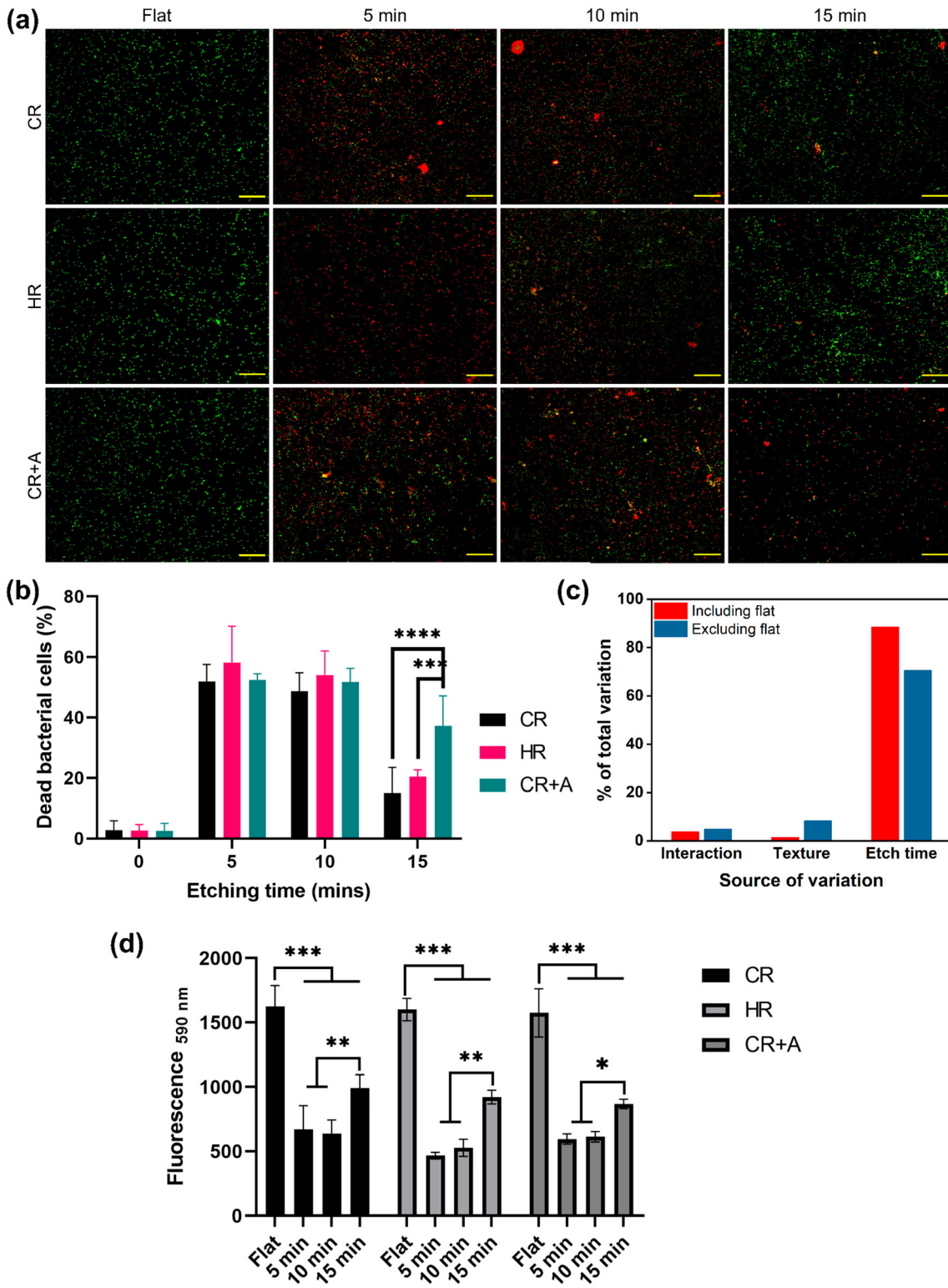
Fig. 4. (a) Representative LIVE/DEAD fluorescent micrographs of flat and nanostructured sample surfaces tested for bactericidal activity; scale bars 50 μm. (b) Grouped bar plot of the percentage of dead bacterial cells on each surface as evaluated from LIVE/DEAD micrographs. (c) Grouped column plot showing the contribution of the two independent variables, texture and etch time, towards determining variation in data in (b). Detailed statistical comparisons between groups and p values are available in the supporting information (Tables S2 and S4). (d) Metabolic activity of bacterial cells on flat and nanostructured surfaces. ***$p < 0.0001$, **$p < 0.001$, *$p < 0.01$.
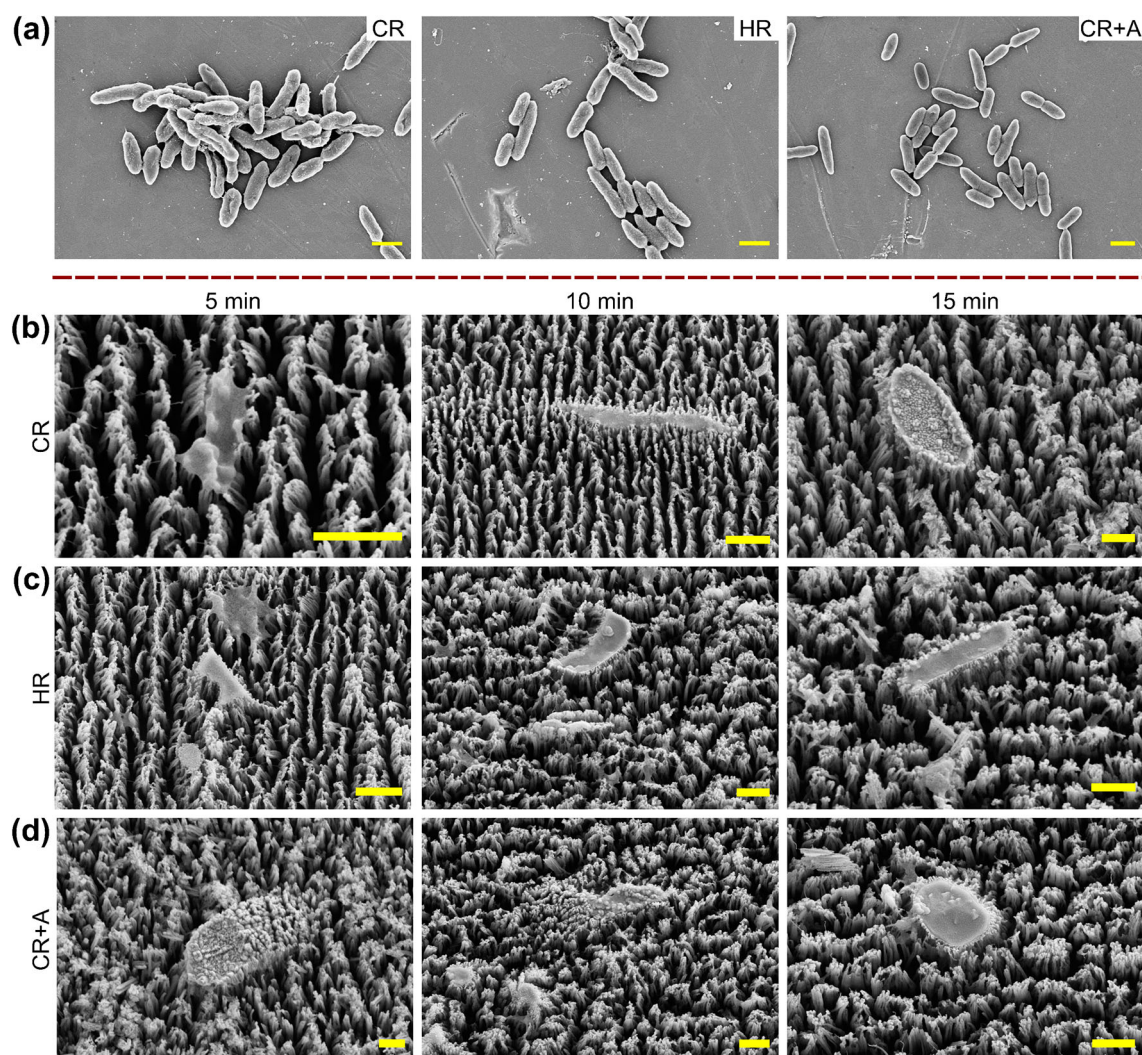
Fig. 5. (a) Microcolonies of *P. aeruginosa* on flat titanium surfaces with different textures. (b–d) Bacterial cell morphology on samples with different textures and etched for varying durations. Cells on surfaces with high BE were found pinned on the nanopillars; note the tent-like deformation of the cell membrane (CR and HR 5 min) and the pillar tips visible through the bacteria (CR + A 5 min, and CR and CR + A 10 min) suggesting that rupture has already occurred, or the bacterial cell partially sunk between nanopillars after losing cell membrane integrity. On samples etched for 15 min, cell membrane integrity has not been lost, and the cell attaches to the pillar tips bending them in the process; scale bars 1 μm.

Other contentious theories suggest that deformation of the cell membrane occurs due to spontaneous adsorption of the cell wall onto the pillar surfaces, which is facilitated by an overall decrease in the free energy of the system.[3] Several bacterial cells were found either partially or completely sunken between the pillars, which could be explained via this mechanism (Fig. 5c). A more recent model has suggested that bacteria experience a net downward pull, due to the presence of an interfacial energy gradient along the pillar length, which might also be responsible for such cellular morphology.[26] A recent review article presents a complete summary of the current theories on interactions that occur at the bacteria–nanostructure interface.[23]

In the case of *S. aureus*, the NSSs did not exhibit any bactericidal activity, and almost all the cells were found alive in the fluorescence micrographs

(Fig. S2). This is consistent with previous reports in the literature, whereby killing efficiency against Gram-positive strains has been found to be lower.[9,10,27] This is attributable to the differences between the structure of the cell walls of Gram-positive and -negative bacteria. There are intrinsic differences between the cell wall structure of Gram-positive and -negative bacteria. Gram-positive bacteria possess a much thicker peptidoglycan layer (20–80 nm) on their cell wall, which acts as a rigid envelope around the cell wall and makes it more difficult to deform or rupture the cell. In contrast, in the case of Gram-negative bacteria, the peptidoglycan layer is much thinner (2–3 nm) and sandwiched between the inner and outer membrane, the latter of which is responsible for protecting the cell against external mechanical stresses. In several recent studies, it has been suggested that, in the case of

Table II. Summary of two-way ANNOVA results showing the contribution of the two factors, texture and etch duration, and the interaction between them towards deciding the bactericidal efficacy of NSSs

Source of variation	% of total variation		p value		p value summary		Significance	
	w/flat	wo/flat	w/flat	wo/flat	w/flat	wo/flat	w/flat	wo/flat
Interaction	3.697	8.294	0.0010	0.0042	**	**	Yes	Yes
Etching time (mins)	88.42	70.57	< 0.0001	< 0.0001	****	****	Yes	Yes
Texture	1.376	4.898	0.0100	0.0087	*	**	Yes	Yes

$w/flat$ including flat surfaces, $wo/flat$ excluding flat surfaces.

Gram-negative bacteria, the delamination of the inner membrane from the outer one can cause the cell to lose its shape, and trigger intracellular reaction cascades for programmed cell death or cause cell death due to loss of cell wall integrity.[28,29] SEM micrographs further confirmed that the *S. aureus* cells on the NSSs were minimally distorted upon interacting with the nanostructures, and were able to maintain their original morphology and cell shape integrity, unlike their Gram-negative counterparts (Fig. S2). Analysis of SEM images further revealed that most of the *S. aureus* cells formed attachments with pillar tips or tip clusters, which is counterintuitive, since it would be more favorable for the cell to settle between the pillars. This is so because, by avoiding direct contact with the pillar tip, the cell can minimize the local strain on its cell wall. In fact, Linklater et al. reported that, in their case, *S. aureus* cells which preferred to settle between nanopillars and surfaces with a hierarchical structure, i.e., with shorter nanopillars between taller tip clusters, had a killing efficacy of around 50%.[10] However, the small interspacing of the nanopillars in our study might have made it difficult for cells to settle between them, thereby forcing them to attach on top of the pillars.

These results underscore the importance of differences between Gram-positive and -negative bacteria, and the necessity to investigate both types of bacteria while evaluating the bactericidal potential of nanotopographies. Moreover, reports have shown that Gram-positive strains such as *S. aureus* are more prevalently found in implant infections than Gram-negative ones, implying that efficacy against such strains is indispensable for clinical translation of this technology.[2]

Finally, the influence of texture on dry etching and subsequently BE has been quantified using statistical analysis. As mentioned above, differences between texture groups for the same etch durations were non-significant, except in the case of samples etched for 15 min. However, a two-way ANOVA test on the bacterial data revealed that the source of variation in the data arising due to interaction between the two independent parameters, texture and etch time, is statistically significant, with a p value of 0.001 (Table S1). Therefore, the bactericidal activity of the substrates was dependent on both these parameters, and this interaction contributed to 3.697% of the total variation. Individually, etching time accounted for the largest contribution to the percentage of total variation (88.42%) with a p value of < 0.0001, and texture accounted for 1.376% with a p value of 0.001 (Fig. 4c; Table II). However, since the variation between the flat substrates belonging to different texture groups was minimal, crystallographic texture by itself did not appear to affect bacterial attachment. Therefore, another analysis of only the NSSs, excluding the data for flat substrates, was conducted to better understand the direct and indirect effects of texture on the dry etching process and BE. Analysis revealed a stronger contribution arising due to the texture of the material, with the contribution of texture increasing to 4.898% (p value 0.0087) and the interaction between etching time and texture contributing 8.294% (p value 0.0042) (Fig. 4c; Table S3). The results of multiple comparisons between different groups, including and excluding flat substrates, are available in the supporting information file (Tables S2 and S4, respectively). Therefore, it can be concluded that crystallographic texture contributes significantly to determining the mechanobactericidal activity of NSSs, due to its direct effects on the formation of nanostructures via the maskless dry-etching process. The true potential of high aspect ratio mechanobactericidal topographies can be realized by the fabrication of bactericidal yet non-cytotoxic surfaces. Micro- and nanoscale features on a surface have been known to provide mechanical stimuli to cells and even play vital roles in directing stem cell fate or aiding attachment and proliferation of osteoblasts. Multiple recent studies have suggested that bactericidal and cytocompatible topographies do exist, although both BE and cytocompatibility are heavily affected by nanostructure dimensions.[9,30,31] A previous study by our group demonstrated that nanopillars generated on titanium by dry etching played a vital role in helping to differentiate human mesenchymal stem cells toward osteoblasts.[9] Further studies on nanostructured titanium have shown that, compared to flat substrates, such nanotopographies can modulate mechanotransduction pathways in cells, by interacting with the cellular cytoskeleton, upregulating several markers associated with increased bone mineralization, and encouraging regeneration.[30,31]

The Significance of Crystallographic Texture in Dry Etching of Titanium to Engineer
Bioinspired Nanostructured Bactericidal Surfaces

3377

CONCLUSION

We have generated nanoscale mechanobactericidal topographies on titanium that had been subjected to different metallurgical processing routes to generate distinct crystallographic textures, and have then investigated their BE against Gram-positive and Gram-negative strains. We found that, while the NSSs were effective in eliminating Gram-positive *P. aeruginosa*, their efficacy against Gram-positive *S. aureus* was negligible. Therefore, the results of our study emphasize the need for exploring nanotopographies with good bactericidal efficiency against both types of bacteria. Moreover, we found statistically significant differences between groups with different textures, and detailed analysis revealed that the contribution of texture is incremented on nanostructured topographies. Our results emphasize the importance of crystallographic texture on the dry etching of titanium, and the use of dry-etched topographies as bactericidal surfaces, and demonstrate that it can prove to be an important tool for enhancing the killing efficiency of bacteria.

ACKNOWLEDGEMENTS

CONFLICT OF INTEREST

The authors declare they have no conflicts of interest.

SUPPLEMENTARY INFORMATION

The online version contains supplementary material available at https://doi.org/10.1007/s11837-022-05395-w.

REFERENCES

1. P. Izakovicova, O. Borens, and A. Trampuz, *EFORT Open Rev.* 4, 482 https://doi.org/10.1302/2058-5241.4.180092 (2019).
2. C.R. Arciola, D. Campoccia, and L. Montanaro, *Nat. Rev. Microbiol.* 16, 397 https://doi.org/10.1038/s41579-018-0019-y (2018).
3. D.P. Linklater, V.A. Baulin, S. Juodkazis, R.J. Crawford, P. Stoodley and E.P. Ivanova, *Nat. Rev. Microbiol.* 19, 1 https://doi.org/10.1038/s41579-020-0414-z (2020).
4. S.L. Lammie and J.M. Hughes, *Annu. Rev. Food Sci. Technol.* 7, 287 https://doi.org/10.1146/annurev-food-041715-033251 (2016).
5. E.P. Ivanova, J. Hasan, H.K. Webb, V.K. Truong, G.S. Watson, J.A. Watson, V.A. Baulin, S. Pogodin, J.Y. Wang, and M.J. Tobin, *Small* 8, 2489 https://doi.org/10.1002/smll.201200528 (2012).
6. J. Hasan, A. Roy, K. Chatterjee, and P.K. Yarlagadda, *ACS Biomater. Sci. Eng.* 5, 3139 https://doi.org/10.1021/acsbiomaterials.9b00217 (2019).
7. E.P. Ivanova, J. Hasan, H.K. Webb, G. Gervinskas, S. Juodkazis, V.K. Truong, A.H. Wu, R.N. Lamb, V.A. Baulin, and G.S. Watson, *Nat. Commun.* 4, 1 https://doi.org/10.1038/ncomms3838 (2013).
8. J. Hasan and K. Chatterjee, *Nanoscale* 7, 15568 https://doi.org/10.1039/C5NR04156B (2015).
9. J. Hasan, S. Jain, and K. Chatterjee, *Sci. Rep.* 7, 1 https://doi.org/10.1038/srep41118 (2017).
10. D.P. Linklater, S. Juodkazis, R. Crawford, and E. Ivanova, *Materialia* 5, 100197 https://doi.org/10.1016/j.mtla.2018.100197 (2019).
11. A. Roy, and K. Chatterjee, *ACS Appl. Nano Mater.* 5, 4447 https://doi.org/10.1021/acsanm.2c00555 (2022).
12. S. Bahl, S. Suwas, and K. Chatterjee, *RSC Adv.* 4, 38078 https://doi.org/10.1039/c4ra05440g (2014).
13. S. Faghihi, F. Azari, H. Li, M.R. Bateni, J.A. Szpunar, H. Vali, and M. Tabrizian, *Biomaterials* 27, 3532 https://doi.org/10.1016/j.biomaterials.2006.02.027 (2006).
14. M. Hoseini, P. Bocher, A. Shahryari, F. Azari, J.A. Szpunar, and H. Vali, *J. Biomed. Mater. Res. Part A* 102, 3631 https://doi.org/10.1002/jbm.a.35028 (2014).
15. B.-Q. Fu, W. Liu, and Z.-L. Li, *Appl. Surf. Sci.* 255, 9348 https://doi.org/10.1016/j.apsusc.2009.07.034 (2009).
16. D. Dictus, D. Shamiryan, V. Paraschiv, W. Boullart, S. De Gendt, and S. Vanhaelemeersch, *J Vac Sci Technol B* 24, 2472 https://doi.org/10.1116/1.2348725 (2006).
17. L. Xie, T.X. Zhou, R.J. Stöhr, and A. Yacoby, *Adv. Mater.* 30, 1705501 https://doi.org/10.1002/adma.201705501 (2018).
18. S. Suwas and R.K. Ray, *Crystallographic Texture of Materials* (Springer, New York, 2014).
19. A. Zeniou, K. Ellinas, A. Olziersky, and E. Gogolides, *Nanotechnology* 25, 035302 https://doi.org/10.1088/0957-4484/25/3/035302 (2013).
20. D. Chandra and S. Yang, *Acc. Chem. Res.* 43, 1080–1091 https://doi.org/10.1021/ar100001a (2010).
21. S. De Bentzmann and P. Plésiat, *Environ. Microbiol.* 13, 1655 https://doi.org/10.1111/j.1462-2920.2011.02469.x (2011).
22. M. Cerioli, C. Batailler, A. Conrad, S. Roux, T. Perpoint, A. Becker, C. Triffault-Fillit, S. Lustig, M.-H. Fessy, and F. Laurent, *Front. Med.* 7, 701 https://doi.org/10.3389/fmed.2020.513242 (2020).
23. A. Roy and K. Chatterjee, *Nanoscale* 13, 647 https://doi.org/10.1039/d0nr07976f (2021).
24. E.P. Ivanova, D.P. Linklater, M. Werner, V.A. Baulin, X. Xu, N. Vrancken, S. Rubanov, E. Hanssen, J. Wandiyanto, V.K. Truong, A. Elbourne, S. Maclaughlin, S. Juodkazis, and R.J. Crawford, *Proc. Natl. Acad. Sci.* 117, 12598 https://doi.org/10.1073/pnas.1916680117 (2020).
25. D.P. Linklater, M. De Volder, V.A. Baulin, M. Werner, S. Jessl, M. Golozar, L. Maggini, S. Rubanov, E. Hanssen, S. Juodkazis, and E.P. Ivanova, *ACS Nano* 12, 6657 https://doi.org/10.1021/acsnano.8b01665 (2018).
26. T. Liu, Q. Cui, Q. Wu, X. Li, K. Song, D. Ge, and S. Guan, *J Phys Chem B* 123, 8686 https://doi.org/10.1021/acs.jpcb.9b07732 (2019).
27. S. Pogodin, J. Hasan, V.A. Baulin, H.K. Webb, V.K. Truong, T.H.P. Nguyen, V. Boshkovikj, C.J. Fluke, G.S. Watson, and J.A. Watson, *Biophys. J.* 104, 835 https://doi.org/10.1016/j.bpj.2012.12.046 (2013).
28. S. Zhao, Z. Li, D.P. Linklater, L. Han, P. Jin, L. Wen, C. Chen, D. Xing, N. Ren, and K. Sun, *Nano Lett.* 22, 1129 (2022).
29. C.D. Bandara, S. Singh, I.O. Afara, A. Wolff, T. Tesfamichael, K. Ostrikov, and A. Oloyede, *ACS Appl. Mater. Interfaces* 9, 6746 https://doi.org/10.1021/acsami.6b13666 (2017).
30. K. Modaresifar, M. Ganjian, L. Angeloni, M. Minneboo, M.K. Ghatkesar, P.L. Hagedoorn, L.E. Fratila-Apachitei, and A.A. Zadpoor, *Small* 17, 2100706 https://doi.org/10.1002/smll.202100706 (2021).

31. T.L. Clainche, D. Linklater, S. Wong, P. Le, S. Juodkazis,
    X.L. Guével, J.-L. Coll, E.P. Ivanova, and V. Martel-Frachet,
    ACS Appl. Mater. Interfaces 12, 48272 https://doi.org/10.10
    21/acsami.0c11502 (2020).

Publisher's Note Springer Nature remains neutral with regard to jurisdictional claims in published maps and institutional affiliations.